



Contents lists available at ScienceDirect

Optik

journal homepage: www.elsevier.com/locate/ijleo

Ultra-broadband visible and mid-infrared light absorber via magnetic dipole and surface plasmon resonances

Tiesheng Wu^{a,b,c}, Xueyu Wang^{b,*}, Huixian Zhang^b, Weiping Cao^b, Yiying Wang^b,
Yiping Wang^{a,c}, Zhihui Liu^b, Dan Yang^b, Zuning Yang^b

^a Key Laboratory of Optoelectronic Devices and Systems of Ministry of Education and Guangdong Province, Shenzhen University, Shenzhen, 518060, China

^b Guangxi Key Laboratory of Wireless Broadband Communication and Signal Processing, Guilin, 541004, China

^c Guangdong and Hong Kong Joint Research Centre for Optical Fiber Sensors, College of Physics and Optoelectronic Engineering, Shenzhen University, Shenzhen, 518060, China

ARTICLE INFO

Keywords:

Metamaterial
Absorber
Ultra-broadband

ABSTRACT

We numerically demonstrate an ultra-broadband plasmonic absorber by applying chromium and titanium in a 3D metamaterial structure. One unit cell of the proposed absorber consists of continuous Cr/SiO₂ multi-layers covered by two Ti nanodisks for exciting multiple magnetic dipole resonances and localized surface plasmon resonance. The optical simulation results show that the average absorption of the plasmonic structure exceeds 98.4% in the wavelength range of 400–4000 nm. The broadband and high absorption benefits from impedance matching between the nanodisks array and the free space in the wavelength range. Through thermal simulation, we also investigated the photothermal heating generation in the plasmonic metamaterial structure. The temperature rise in the proposed structure is approximately 447 K with an incident wavelength of 618 nm and a light flux of 100 W/cm². Due to the ultra-broadband absorbing performance, the presented design has possibilities in the fields of photodetector applications, solar energy harvesting, thermal emitters, and infrared cloaking.

1. Introduction

Plasmonic absorber has been getting much attention due to its potential application prospects [1–3]. It can be used in many promising fields, such as plasma light-harvesting [4,5], spectral filters [6–9], solar photovoltaic power generation [10–14], thermal radiometers [15,16]. Because of the absorption efficiency and bandwidth cannot meet the requirements, most plasmonic absorbers are limited in practical applications. To overcome these disadvantages, Landy proposed and evidenced a perfect metamaterial absorber for the first time [17]. Zhu et al. designed a multi-layered complex structure of gold and silicon, and the average absorption of this structure can get 95 % for a bandwidth of 1700 nm [18]. Deng et al. presented a broadband absorber by tapered hyperbolic multilayer waveguides, and its average absorption exceeds 92 % in the range of 1000–6000 nm [19]. Wu et al. put forward a hollowed-out multi-layer ultra-wideband absorber with an average absorption above 97.8 % in the wavelength range from 40 to 1500 nm [20]. By adding an ultra-thin titanium nitride, Liu et al. demonstrated a broadband absorber with average absorption exceeding 97 % for the 316–1426 nm range [21]. Despite the great success of the above reports in the broadband absorber designing, it is still challenging to achieve ultra-broadband absorption of visible and mid-infrared light with high efficiency for the real application

* Corresponding author.

E-mail addresses: wxyfyz@163.com (X. Wang), ypwang@szu.edu.cn (Y. Wang).

<https://doi.org/10.1016/j.ijleo.2020.165142>

Received 7 February 2020; Received in revised form 8 June 2020; Accepted 14 June 2020
0030-4026/ © 2020 Published by Elsevier GmbH.

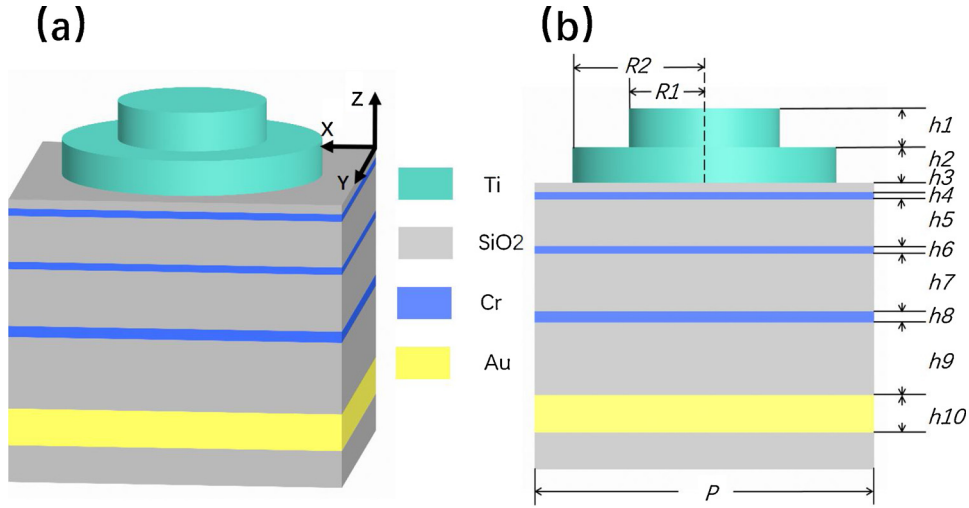


Fig. 1. (a) Three-dimensional schematic and (b) cross-section of the proposed absorber.

environment.

In this paper, we have proposed and numerically investigated an ultra-broadband perfect absorber for absorbing visible light and mid-infrared light (400–4000 nm). The proposed absorber consists of alternating chromium/silica (Cr/SiO₂) planar films capped by periodical nanodisks. First, a schematic diagram of the proposed absorber based on multiple magnetic dipole resonances and localized surface plasmon resonance (LSPR) is presented. Then optical simulation is performed to investigate the absorption characteristics of the metamaterial structure by using the finite difference time domain (FDTD) method and the finite element method (FEM). The proposed absorber demonstrates excellent performance in terms of wide bandwidth and high absorbing efficiency, simultaneously. The average absorption reaches 98.4 % for the 400–4000 nm wavelength range. As far as we know, the previously reported either the average absorption efficiency is close to that of this work, but the bandwidth is much smaller; or even reach such a large bandwidth, but the average absorption efficiency is several percentage points lower. Finally, the effect of photothermal heating in the plasmonic nanostructure is analyzed through thermal simulation.

2. Design and simulation methods

Fig. 1(a) illustrates one unit cell of the plasmonic absorber. Two vertically stacked metal nanodisks are placed on the alternating multilayered (SiO₂/metal) continuous films. For convenience, the proposed absorber is abbreviated as TGSA (Ti-Cr-SiO₂ absorber). The substrate is set as a quartz substrate with a thickness of 250 μm. The cross-sectional view of the structure is shown in Fig. 1(b), the thickness and radius of the upper Ti nanodisk are h_1 and R_1 , respectively. The thickness and radius of the lower Ti nanodisk are denoted by h_2 and R_2 , respectively. P denotes the lattice constant of the metamaterial structure. In the following simulation, P is set to be a constant with a value of 180 nm both in the x and y axes. From top to bottom, the thicknesses of the SiO₂ layers which are spaced by Cr films are denoted by h_3 , h_5 , h_7 , and h_9 , respectively. The thickness of the three layers of Cr films are set as h_4 , h_6 , and h_8 , respectively. The bottom layer is an Au layer with a thickness of $h_{10} = 300$ nm, and it is used as a reflective layer for improving absorption efficiency.

In the optical simulation, three-dimensional (3D) FDTD method is used to investigate its absorption characteristics. The boundaries along the x and y axes are set as periodic boundary conditions, and the boundary at the z-direction is set as perfectly matching layers (PML). In order to get more accurate simulation results, we did convergence testing for FDTD simulations. The mesh sizes are set to be 5×5 nm for the x and y directions, and 1 nm for the z-direction, under this condition, the simulation results are convergent. The refractive indexes of these materials used in the simulation are derived from experimental data [22,23]. The absorber is normally illuminated by a TM-polarized planar wave with the propagation direction along the negative z-direction. A power monitor is placed directly above the light source to calculate the normalized reflection $R(\lambda)$. As the Au layer in the bottom is sufficiently thicker than the penetration depth in the wavelength range, the transmission of the absorber is zero. Therefore, the absorption can be represented as $A(\lambda) = 1 - R(\lambda)$. The average absorption can be calculated as [24,25]

$$A = \int_{\lambda_1}^{\lambda_2} A(\lambda) d\lambda / (\lambda_2 - \lambda_1) \quad (1)$$

Where λ_1 and λ_2 are set to be 400 and 4000 nm, respectively.

We also perform thermal simulation for investigating photothermal heating in the proposed structure. The regions of thermal simulation and optical simulation are identical in the x and y directions. But not the same, the thermal simulation involves the entire thickness of the substrate for modelling the heat propagation through the quartz substrate. The boundary in the positive z-direction is set as a convective boundary condition with a convective heat transfer coefficient $h = 10$ W/m²K. The boundary condition at the

bottom is set as a fixed temperature thermal boundary condition (300 K). The optical simulation results are imported into the thermal simulation module as an import heat source. A temperature monitor is placed surrounding the proposed metamaterial absorber to record the temperature profile.

In order to better explain the ultra-broadband and high absorption performance, the impedance of the proposed structure is detailed calculated and analyzed based on the impedance transformation method. According to [26,27], the impedance can be derived from the S parameters as

$$Z = \pm \sqrt{\frac{(1 + S_{11})^2 - S_{21}^2}{(1 - S_{11})^2 - S_{21}^2}} \quad (2)$$

Because the transmission of the absorber is zero, the parameter $S_{21} = 0$. Hence, the Eq.(2) can be abbreviated as [28,29]

$$Z = \pm \frac{|1 + S_{11}|}{|1 - S_{11}|} \quad (3)$$

It is well known that the S_{11} can be obtained by

$$S_{11} = \sqrt{R(\lambda)} \quad (4)$$

Hence, the impedance Z of the proposed structure is yielded by

$$Z = \pm \frac{|1 + \sqrt{R(\lambda)}|}{|1 - \sqrt{R(\lambda)}|} \quad (5)$$

3. Results and discussion

Fig. 2 (red curve) illustrates the absorption efficiency as a function of incident wavelength for the proposed structure. In the simulation, the parameters are set as $P = P_x = P_y = 180$ nm, $h_1 = 261$ nm, $R_1 = 50$ nm, $h_2 = 200$ nm, $R_2 = 70$ nm, $h_3 = 5$ nm, $h_4 = 4$ nm, $h_5 = 230$ nm, $h_6 = 5$ nm, $h_7 = 360$ nm, $h_8 = 12$ nm, $h_9 = 355$ nm, and $h_{10} = 200$ nm, respectively. In the following analysis, if not specified, the parameters are unchanged. As shown in Fig. 2, we can see that the lowest absorption efficiency is over 86.2 % for the entire simulation wavelength range. Calculated according to Eq. (1), the average absorption efficiency reaches up to 98.4 % in the wavelength range of 400 – 4000 nm. What's more, the lowest absorption efficiency achieves 99.1 %, and the average absorption exceeds 99.6 % for the range of 1200 – 3700 nm. Whether from absorption efficiency or perfect absorption bandwidth, the absorption performance of the proposed absorber is significantly better than most of the previously published works. In previous reports, most of the absorbers used precious metals (gold or silver) as the absorbing material. For comparison, we replaced the chromium in this structure with gold. The similar absorber is abbreviated as TGSA (Ti-Gold- SiO₂ absorber). Fig. 2 (green curve) shows the absorption spectra of the TGSA. As shown in Fig. 2, when the wavelength is greater than 1480 nm, the absorption efficiency of the TGSA decreases sharply with increasing wavelength. The comparison results indicate the rationality and superiority of the proposed structure for ultra-broadband absorbing. In addition, in order to ensure the reliability and accuracy of the calculation results, the absorption spectra of the TCSA is also simulated by using the finite element method (FEM) (see Fig. 2 black curve). The FEM simulation is performed with a commercial software Comsol. The results obtained by the two simulation methods are slightly different, but the trend of absorption efficiency with wavelength is the same, indicating that our FDTD simulation results are reliable.

Impedance matching is the prerequisite for perfect absorption because a better impedance matching can reduce the reflection of light. In principle, the impedance matching situation is closely related to material properties and structure dimensions. As we all know, the impedance of free space is $Z_0(\omega) = \sqrt{\mu(\omega)/\varepsilon(\omega)} = 1$ [30]. For achieving ultra-broadband perfect absorption, the impedance matching should be achieved at the entire working wavelength, that is, satisfy the condition $Z = Z_0$. According to Eq. (5), we

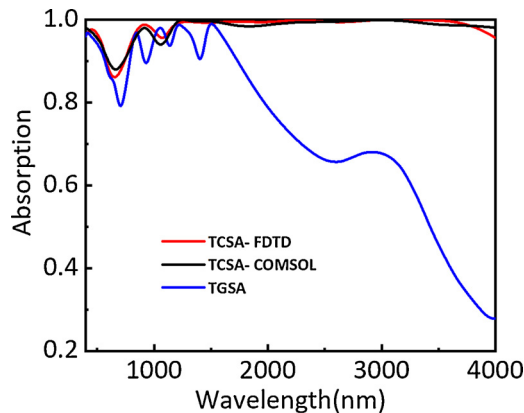


Fig. 2. Absorption characteristics of the TCSA and TGSA structure versus the incident wavelength.

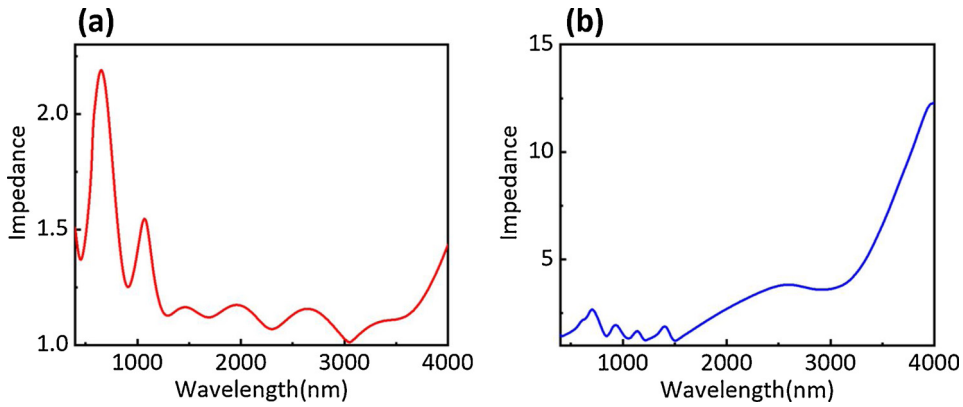


Fig. 3. Impedance versus the incident wavelength. (a) TCSA structure, and (b) TGSA structure.

calculated the impedance curves of TCSA and TGSA. The relationship between the impedance and the incident wavelength for TCSA is shown in Fig. 3(a). The result shows that the impedance of TCSA is close to 1 with a range of 1200–3700 nm, which is consistent with the perfect absorption wavelength range, as shown in Fig. 2 (red curve). Fig. 3(b) illustrates the impedance matching situation for the TGSA structure. The TGSA structure has a good impedance matching situation only in the range of 400–1200 nm. Obviously, the different material properties of the two structures cause a distinct difference in the absorption efficiency.

In order to elucidate the physical mechanism of the proposed ultra-broadband absorber, we investigate the magnetic field distributions in the x - z plane for six different wavelengths. The normally incident light is set as a TM-polarized wave, and the wavelengths are taken as 400, 491, 673, 992, 3134 and 4000 nm, respectively. Fig. 4(a–f) plot the distributions of magnetic fields at the six different wavelengths. At the resonance wavelength of 400 nm (see Fig. 4a), we can see that the magnetic field is mainly located near the upper surface of the upper Ti nanodisk. Such field distribution corresponds to the excitation of a magnetic dipole resonance, which steps from the near-field plasmon hybridization between the upper nanodisk and the surrounding air. As shown in Fig. 4(b) and (c), with the wavelength increases, the magnetic fields are mainly concentrated around the two nanodisks. This shows that the magnetic dipole resonance is simultaneously excited in the lower nanodisk. According to the magnetic field distributions at the wavelength of 992 nm (see Fig. 4d), we can see that three magnetic dipole resonances are excited and overlapped in the proposed structure. At the wavelength of 4000 nm (see Fig. 4f), the magnetic field is mainly located in the first SiO₂ layer between the lower nanodisk and the thin Cr layer, which indicate that the absorption at this wavelength originating from the excitation of the localized surface plasmon (LSP) resonance. In summary, the interaction of multiple magnetic dipole resonances and LSP causes ultra-

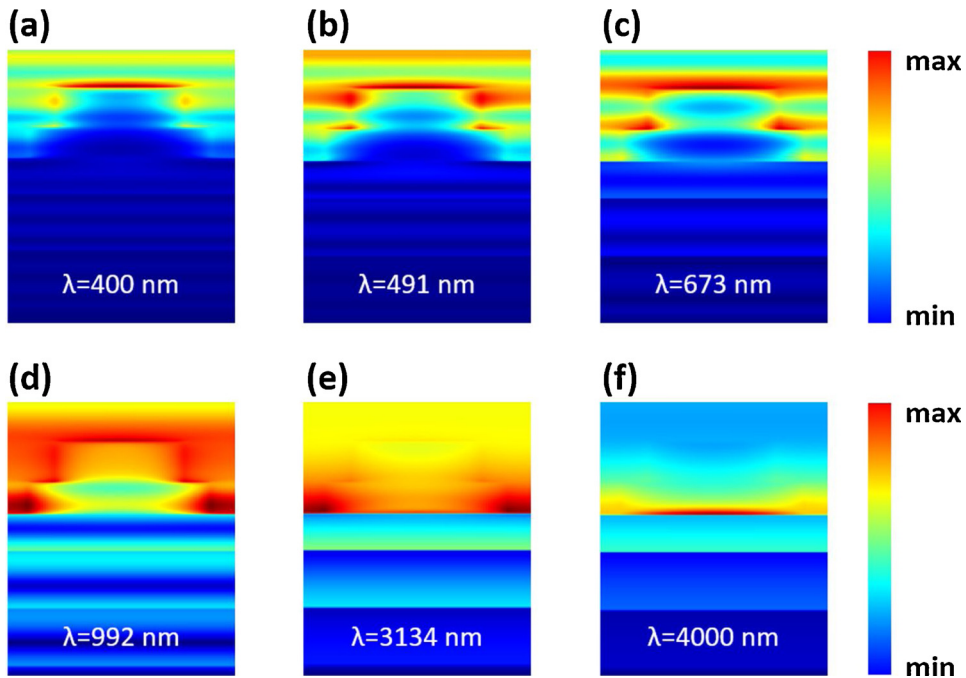


Fig. 4. (a–f) Magnetic field distributions in the x - z plane for different wavelengths.

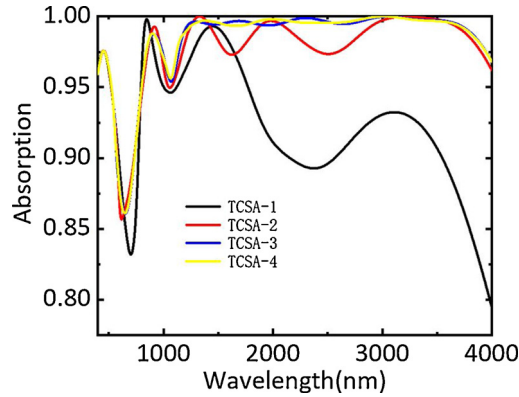


Fig. 5. Absorption spectra for TCSA. TCSA-1, 2, 3, and 4 correspond to the number of the metal chromium layers.

broadband perfect absorption in the structure.

In order to analyze the effect of Cr-layers on absorption efficiency, we calculate the absorption efficiency of the TCSA structure with different Cr-layers. For convenience, the absorber with one layer of metallic Cr is abbreviated as TCSA-1 ($h_5 \sim h_9$ are all set to 0 in the simulation), and so on. As shown in Fig. 5, we can see that the absorption efficiency of TCSA-1 is the worst. Compared with TCSA-2, TCSA-3, and TCSA-4, the absorption efficiency of TCSA-1 is significantly lower in the wavelength range of 1650–4000 nm. Its absorption efficiency decreases at first, and then increases, and finally decreases in this wavelength range. In the range of 400–1300 nm, there is no significant difference in the absorption performances for the four structures. Compared with TCSA-3 and TCSA-4, the absorption spectra of TCSA-2 is not so smooth in the range of 1300–3100 nm. For the range of 400–4000 nm, the average absorptions of the four structures are 92.13 %, 97.82 %, 98.42 %, and 98.42 %, respectively. The average absorption of TCSA-3 is equal to that of TCSA-4 in this wavelength range. Thence, it is reasonable to set 3 Cr-layers for the proposed structure.

The effect of the thickness of Cr-layers on the absorption characteristics is also investigated, and the results are shown in Fig. 6(a–f). From Fig. 6(a), (c), and (e), we can see that the thickness variation of the Cr-layers has little effect on the absorption efficiency in the short wavelength range. But, it affects the absorption characteristics for the wavelength greater than 1000 nm. Compared to the thickness of h_6 and h_8 , the change of thickness h_4 has a greater influence on the absorption characteristics, especially the absorption bandwidth. When one of the thickness h_4 , h_6 , h_8 increases from 0 to 20 nm, the average absorption increases first and then decreases, and the results are shown in Fig. 6(b), (d) and (f), respectively. For the structural parameter h_4 , the average absorption reaches the maximum when $h_4 = 4$ nm. The change of h_4 mainly affects the light absorption for the wavelength range 3000–4000 nm. For the thickness h_6 , the average absorption reaches the maximum when h_6 equals to 5 nm. The h_6 changes from 0 to 7 nm, which affects the absorption characteristics of light waves around 2800 nm. When h_6 is greater than 7 nm, the change of the thickness slightly affects light absorption in the range of 3700–4000 nm. Similarly, we can see that the average absorption reaches the maximum when h_8 equals to 12 nm. When the thickness h_8 increased in the range of 0–12 nm, the absorption efficiency also gradually increasing in the wavelength range of 1800–2600 nm. However, the thickness change has little effect on light absorption when the value of h_8 is greater than 12 nm.

Fig. 7(a–h) demonstrate the effect of the thickness of the SiO₂ layer on the absorption characteristics. The influence of the thickness h_3 on the absorption efficiency and average absorption are shown in Fig. 7(a) and (b), respectively. The average absorption efficiency increases first and then decreases with increasing the thickness h_3 . The average absorption efficiency reaches the maximum when h_3 equals to 5 nm. Simultaneously, it is evident that the absorption in the mid-infrared region becomes better, and absorption bandwidth becomes wider. As shown in Fig. 7(c), the influence of the thickness h_5 on the absorption efficiency at different wavelengths is also investigated. It is observed that the absorption broadband becomes wider with increasing the thickness h_5 . However, the average absorption efficiency does not always increase with increasing the thickness h_5 . The structure can obtain the maximum average absorption when $h_5 = 230$ nm. Similarly, we calculated the light absorption as a function of the h_7 and h_9 , and the results are shown in Fig. 7(e–h), respectively. The physical mechanism can be understood as a change in the thickness of the SiO₂ layers, causing the lossy FP resonance wavelength varieties, thereby resulting in a change in the light absorption.

Fig. 8(a) and (c) depict the absorption efficiency as functions of the radius R_1 and the thickness h_1 , respectively. The variation range of the radius R_1 is from 0 to 90 nm. When $R_1 = 90$ nm, it means that the adjacent nanodisks are close together ($P = 180$ nm). As shown in Fig. 8(a), we can see that the proposed absorber has a broader absorption bandwidth when the radius R_1 is in the range of 40–60 nm. For the entire wavelength simulation range, the absorption efficiency is significantly reduced when R_1 increases from 60 to 90 nm. As the radius increases, the average absorption efficiency increases first and then decreases (see Fig. 8(b)). When the radius R_1 is greater than 65 nm, the average absorption decreases sharply with increasing R_1 . The average absorption efficiency is only 53.1 % when R_1 is set as 90 nm. From Fig. 8(c) we can see that the change in thickness h_1 will affect the light absorption, especially when the wavelength of incident light is less than 1000 nm. The average absorption efficiency reaches the maximum when the thickness h_1 equals 261 nm (see Fig. 8(d)). Similarly, we also investigated the effect of the structural parameters of the bottom nanodisk on the light absorption, and the simulation results demonstrate in Fig. 8(e–h). In short, the absorption efficiency of the proposed structure is related to the structural parameters. When the structure parameters of the plasmonic absorber are set as $h_1 = 261$ nm, $R_1 = 50$ nm,

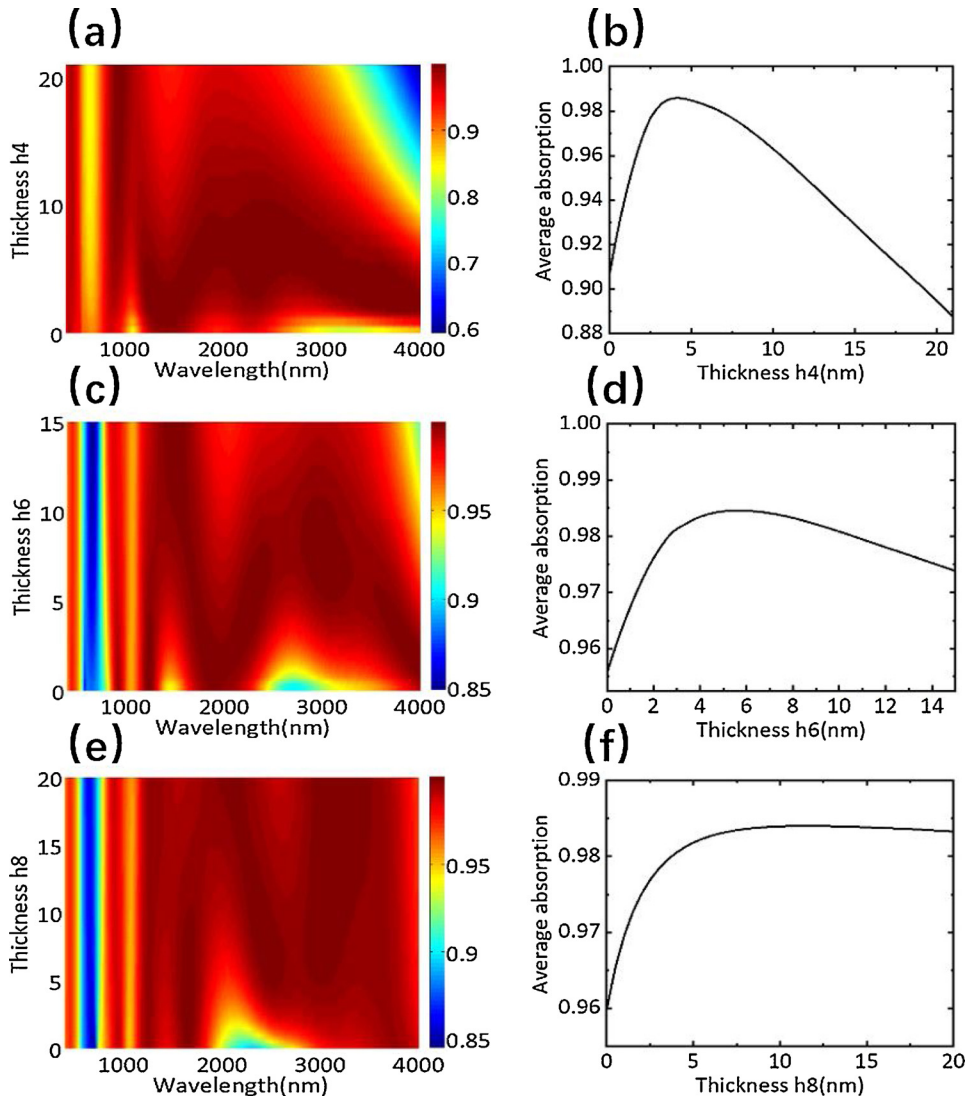


Fig. 6. (a), (c), and (e) Absorption versus the thickness of h_4 , h_6 , and h_8 in the TCSA structure, respectively. (b), (d), and (f) Average absorption versus the thickness of Cr layers.

$h_2 = 200$ nm, $R_2 = 70$ nm, $h_3 = 5$ nm, $h_4 = 4$ nm, $h_5 = 230$ nm, $h_6 = 5$ nm, $h_7 = 360$ nm, $h_8 = 12$ nm, $h_9 = 355$ nm, and $h_{10} = 200$ nm, the average absorption of the proposed structure reaches up to 98.4 % in the range of 400–4000 nm.

For collecting more light energy in practical applications, we also investigated the effect of oblique incidence on the light absorption. The absorption spectra of the absorber with oblique incidences for TE and TM-polarized light are compared and illustrated in Fig. 9(a) and (b), respectively. When the light is a normal incident wave ($\theta = 0^\circ$), the absorption efficiency is independent of the polarization of incident light. For both the TE and TM cases, the average absorption efficiency of the proposed absorber decreases with increasing the incident angle. When the incident angle is $\theta = 60^\circ$, the average absorption efficiencies are 93.1 % and 87.3 %, respectively. As shown in Fig. 7(a) and (b), the longer the wavelength, the more the absorption efficiency is affected by the incidence angle. The physical phenomena is that as the incident angle increases, the more magnetic field is distributed in the air around the nanodisks for the longer wavelengths. When θ equals 60° , for the TE case, the light absorption efficiency at a wavelength of 4000 nm is 76.5 %. For the TM case, the absorption efficiency is 58.2 %. Compared to the TE wave, the oblique incidence of the TM wave has a greater impact on the absorption efficiency, especially in the wavelength range of 3000–4000 nm.

Furthermore, we also investigated the photothermal effect in the plasmonic absorber by using the thermal simulation [31–33]. In the simulation, the thermal conductivities of Au, Ti, Cr, and SiO₂ are set as $k_{Au} = 316$ W/(m·K), $k_{Ti} = 15.6$ W/(m·K), $k_{Cr} = 90$ W/(m·K), $k_{SiO_2} = 0.2$ W/(m·K), respectively. The thermal capacities of these materials are $C_{Au} = 129$ J/(kg·K), $C_{Ti} = 540$ J/(kg·K), $C_{Cr} = 460$ J/(kg·K), $C_{SiO_2} = 200$ J/(kg·K), respectively. Fig. 10(a) shows the temperature rise for one unit cell as a function of input optical power at different resonance wavelengths (i.e., 400 nm, 618 nm, 2254 nm, and 4000 nm). We can see that the temperature rise of the absorber has a linear relationship with the input optical power. Given the same input power, the proposed structure has different

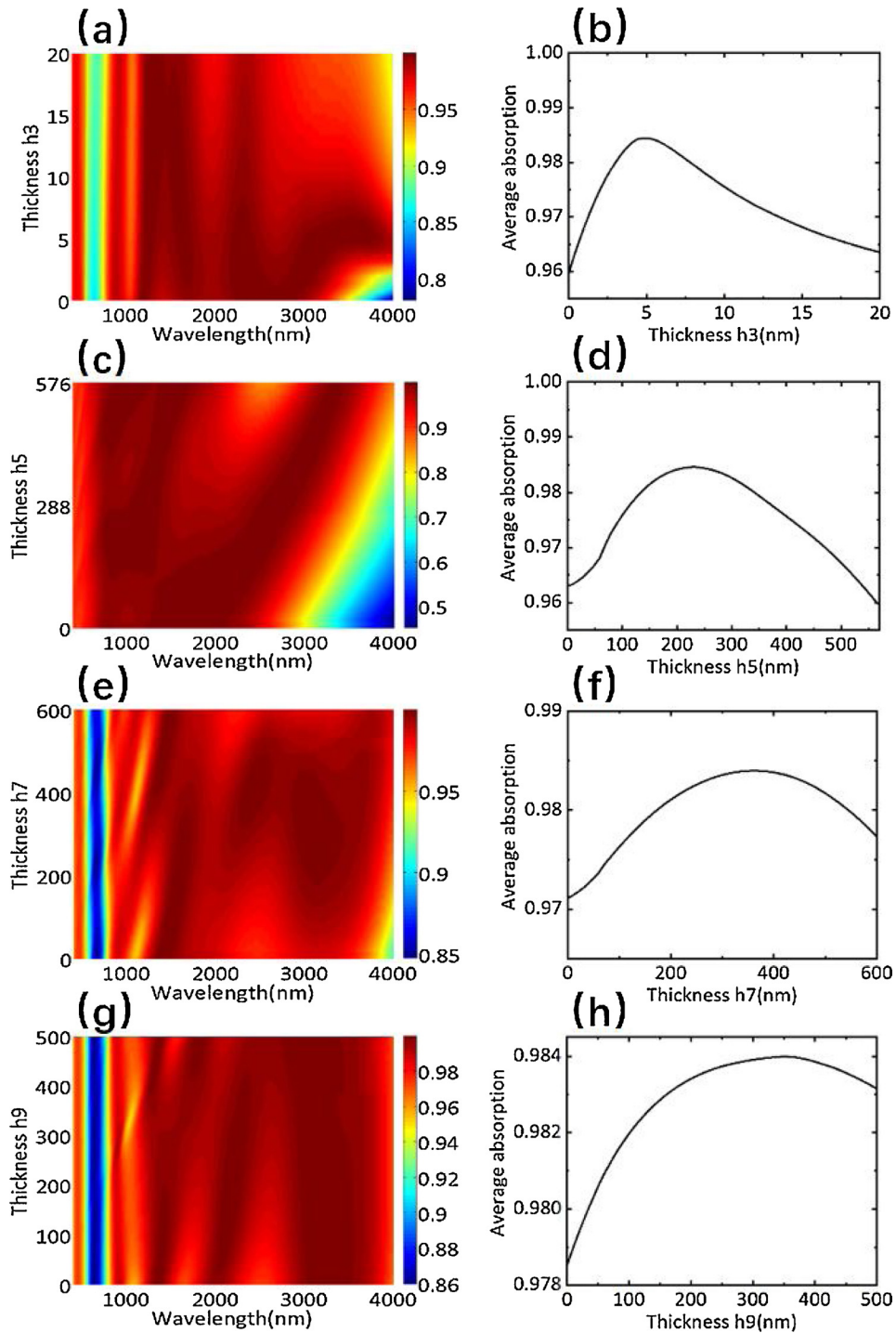


Fig. 7. (a), (c), (e), and (g) Absorption versus the thickness of h_3 , h_5 , h_7 , and h_9 in the TCSA structure, respectively. (b), (d), (f), and (h) Average absorption versus the thickness of the dielectric layers.

temperature rises at different wavelengths due to different absorption efficiency. When the input light flux is 300 W/cm^2 , the temperature rise exceeds 500 K for the incident wavelengths 2254 and 4000 nm . The temperature distribution field is calculated for the incident wavelength of 618 nm with a light flux of 100 W/cm^2 (insert in Fig. 10(a)). When the temperature reaches a steady-state, the temperature at the upper of the structure is slightly higher than the temperature at the lower end. The temperature difference is about 0.4 K . Fig. 10(b) illustrates the temperature rise as a function of incident light wavelength in the range of $400 - 4000 \text{ nm}$. The proposed structure can effectively absorb incident light and convert them into thermal energy with a wide wavelength range. As the

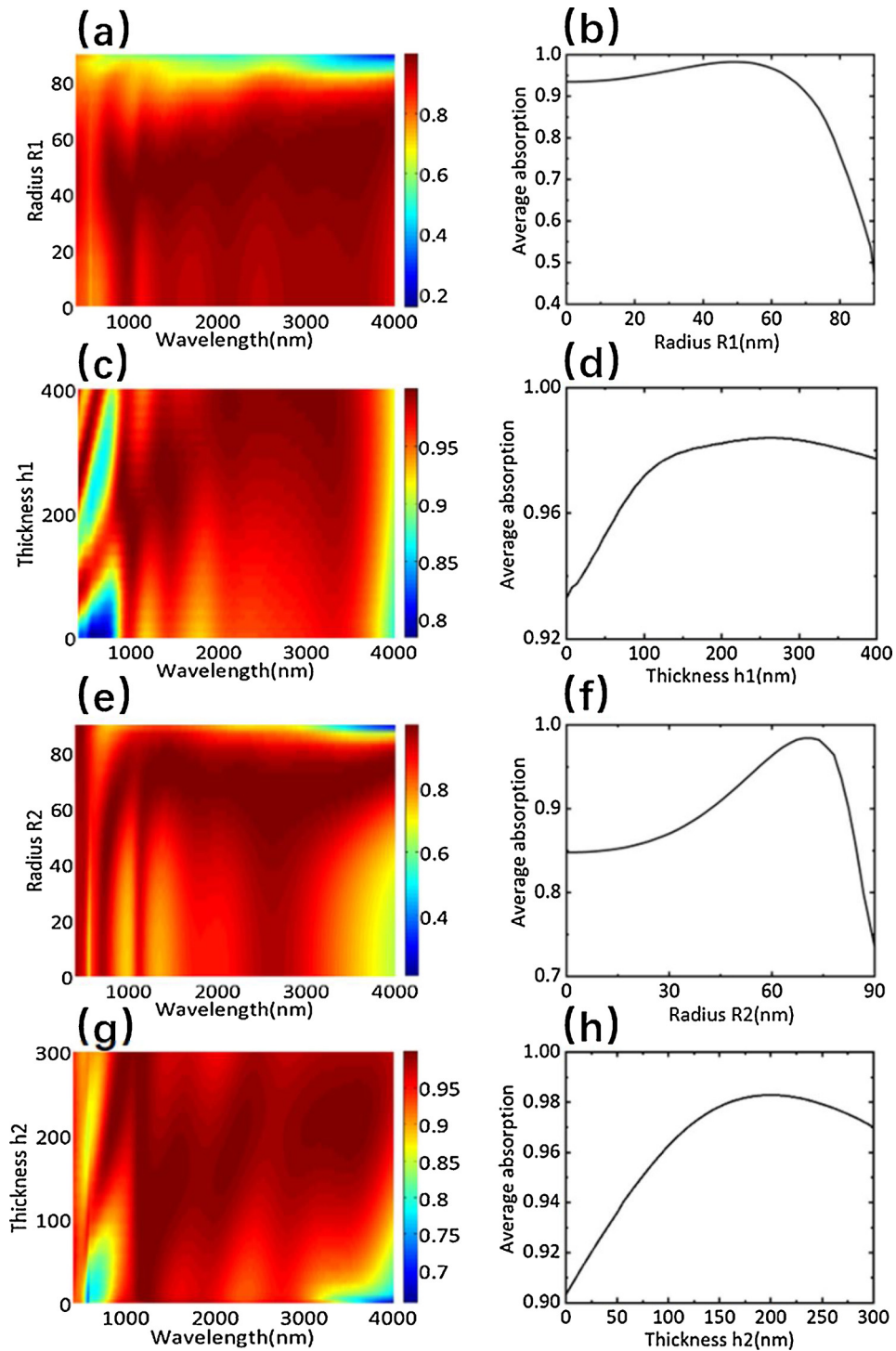


Fig. 8. Absorption spectra varying with (a) radius R_1 , (c) thickness h_1 , (e) radius R_2 , and (g) thickness h_2 in the TCSEA structure. Average absorption efficiency versus (b) radius R_1 , (d) thickness h_1 , (f) radius R_2 , and (h) thickness h_2 in the TCSEA structure, respectively.

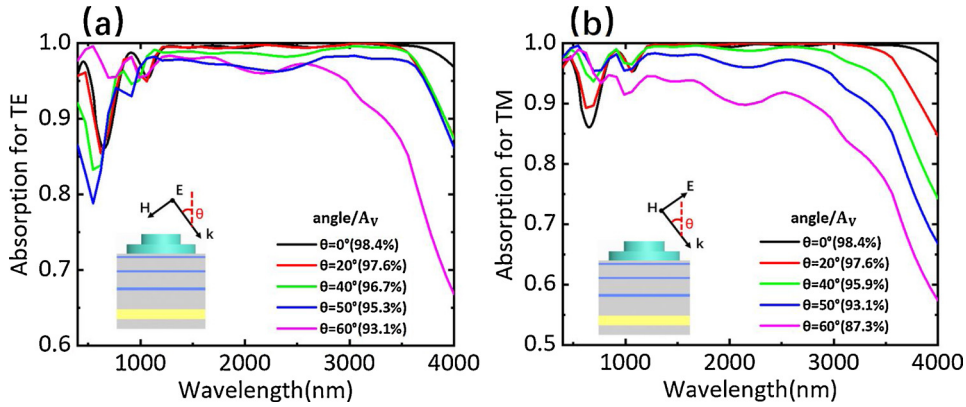


Fig. 9. Absorption efficiency versus wavelength for (a) TE and (b) TM-polarization light incidence with different incident angles.

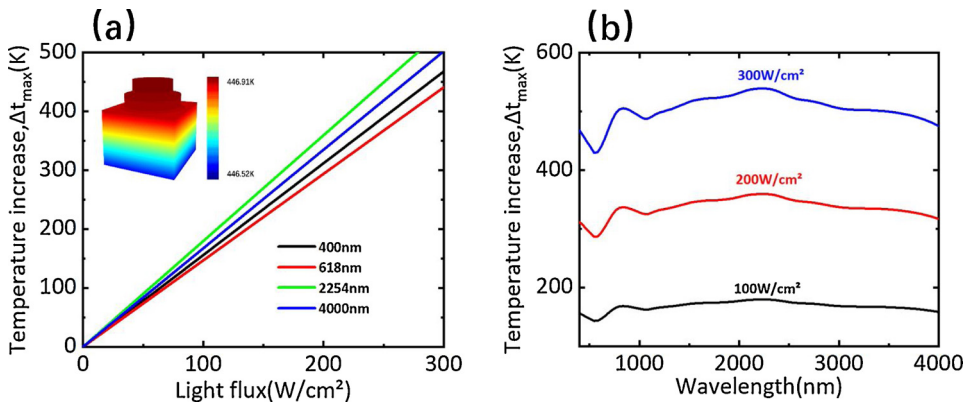


Fig. 10. (a) The temperature rise as a function of input power at different incident wavelengths. (b) The temperature rise versus incident wavelength for different input power.

input power increases, the difference in temperature rise caused by different incident wavelengths becomes more obvious. So proposed the absorber is useful in the application of thermal energy harvesting.

4. Conclusions

In conclusion, we present and demonstrate an ultra-broadband absorber in the visible and mid-infrared region. The proposed absorber is composed of two titanium nanodisks and multi-layers SiO₂/Cr. We investigate its light absorption characteristics by the 3D FDTD method and its photothermal heating effect by the heat transport method, respectively. By optimizing the structural parameters, the average absorption of the proposed structure exceeds 98.4 % for the 400 – 4000 nm wavelength range. The thermal simulation results prove that the proposed structure has high photothermal conversion efficiency in the visible to mid-infrared light region. The temperature rise reaches approximately 447 K for giving an incident wavelength of 618 nm and a light flux of 100 W/cm². The merits of near-perfect absorption efficiency and large absorption bandwidth, make the proposed absorber having potential applications in the field of solar energy harvesting and thermal emitters.

Funding

National Nature Science Foundation of China (61805051); Natural Science Foundation of Guangxi Province (2018JJB170035, 2018AD19071, 2018AD19064, 2018JJA170021) and Supported by the Dean Project of Guangxi Key Laboratory of Wireless Broadband Communication and Signal Processing (GXKL06190118, GXKL06160102, GXKL06180203, GXKL06180104).

Declaration of Competing Interest

The authors declare no conflicts of interest.

References

- [1] J. Liu, W. Chen, J.C. Zheng, Y.S. Chen, C.F. Yang, Wide-angle polarization-independent ultra-broadband absorber from visible to infrared, *Nanomaterials* 10 (27) (2020) 1–17.
- [2] Q.L. Hong, J. Luo, C.C. Wen, J.F. Zhang, Z.H. Zhu, Hybrid metal-graphene plasmonic sensor for multi-spectral sensing in both near- and mid-infrared ranges, *Opt. Express* 27 (24) (2019) 35914–35924.
- [3] N. Gasimov, M. Karaaslan, C. Sabah, F. Karadag, Some aspects of mass-energy equivalence which appears in left-handed metamaterials, *Epj Appl. Metamater.* 6 (2019) 16.
- [4] Y. Li, L. Yue, Y. Luo, W. Liu, M. Li, Light harvesting of silicon nanostructure for solar cells application, *Opt. Express* 24 (14) (2016) A1075–A1082.
- [5] W. Shin, S. Yang, D. Kwon, S. Han, Self-reverse-biased solar panel optical receiver for simultaneous visible light communication and energy harvesting, *Opt. Express* 24 (2016) A1300–A1305.
- [6] M. Bakır, M. Karaaslan, F. Karadag, S. Dalgac, E. Ünal, O. Akgöl, Metamaterial sensor for transformer oil, and microfluidics, *Appl. Comput. Electromagn. Soc. J.* 34 (5) (2019) 799–806.
- [7] M. Bakır, Ş. Dalgac, E. Ünal, F. Karadag, M. Demirci, A.S. Köksal, M. Karaaslan, High sensitive metamaterial sensor for water treatment centres, *Water Air Soil Pollut.* 230 (12) (2019) 304.
- [8] Yadgar I. Abdulkarim, L.W. Deng, K. Muharrem, et al., Novel metamaterials-based hypersensitized liquid sensor integrating omega-shaped resonator with microstrip transmission line, *Sensors* 20 (3) (2020) 943.
- [9] A.S. Feng, Z.J. Yu, X.K. Sun, Ultranarrow-band metagrating absorbers for sensing and modulation, *Opt. Express* 26 (22) (2018) 28197–28205.
- [10] Y. Fu, A. Dinku, Y. Hara, C. Miller, K. Vrouwenvelder, R. Lopez, Modeling photovoltaic performance in periodic patterned colloidal quantum dot solar cells, *Opt. Express* 23 (2015) A779–A790.
- [11] E. Merkkx, O. ten Kate, E. van der Kolk, Rapid optimization of large-scale luminescent solar concentrators: evaluation for adoption in the built environment, *Opt. Express* 25 (2017) A547–A563.
- [12] J. Zhou, Y. Wu, Z. Xia, X. Qin, Z. Zhang, Toward high performance nanoscale optoelectronic devices: super solar energy harvesting in single standing core-shell nanowire, *Opt. Express* 25 (2017) A1111–A1123.
- [13] Y. Song, Y. Jeong, C. Yeo, Y. Lee, Enhanced power generation in concentrated photovoltaics using broadband antireflective coverglasses with moth eye structures, *Opt. Express* 20 (2012) A916–A923.
- [14] L. Zhu, Y. Wang, Y. Liu, C. Yue, Design and analysis of ultra broadband nano-absorber for solar energy harvesting, *Plasmonics* 13 (2) (2018) 475–481.
- [15] H. Deng, C. Mathai, S. Gangopadhyay, J. Gao, X. Yang, Ultra-broadband infrared absorption by tapered hyperbolic multilayer waveguides, *Opt. Express* 26 (2018) 6360–6370.
- [16] G. Liu, J. Chen, P. Pan, Z. Liu, Hybrid metal-semiconductor meta-surface based photo-electronic perfect absorber, *IEEE J. Sel. Top. Quantum Electron.* 25 (3) (2019) 1–7.
- [17] N.I. Landy, S. Sajuyigbe, J.J. Mock, D.R. Smith, W.J. Padilla, Perfect metamaterial absorber, *Phys. Rev. Lett.* 100 (20) (2008) 207402.
- [18] Z. Xu, D. Wu, Y. Liu, C. Liu, Z. Yu, L. Yu, H. Ye, Tunable broad-band perfect absorber by exciting of local surface plasma modes resonances at terahertz frequency, *Nanoscale Res. Lett.* 13 (1) (2019) 143.
- [19] H. Deng, C. Mathai, S. Gangopadhyay, J. Gao, X. Yang, Ultra-broadband infrared absorption by tapered hyperbolic multilayer waveguides, *Opt. Express* 26 (2018) 6360–6370.
- [20] D. Wu, C. Liu, Y. Liu, Z. Xu, Z. Yu, L. Yu, L. Chen, R. Ma, J. Zhang, H. Yea, Numerical study of a wide-angle polarization-independent ultra-broadband efficient selective metamaterial absorber for near-ideal solar thermal energy conversion, *RSC Adv.* 8 (38) (2018) 21054–21064.
- [21] Z. Liu, G. Liu, Z. Huang, et al., Ultra-broadband perfect solar absorber by an ultra-thin refractory titanium nitride meta-surface, *Sol. Energy Mater. Sol. Cells* (2017) S0927024817306815.
- [22] Edward D. Palik, *Handbook of Optical Constants of Solids*, (1985).
- [23] P.B. Johnson, R.W. Christy, Optical constants of the noble metals, *Phys. Rev. B* 6 (12) (1972) 4370–4379.
- [24] H. Gao, W. Peng, S. Chu, W. Cui, Z. Liu, L. Yu, Z. Jing, Refractory ultra-broadband perfect absorber from visible to near-infrared, *Nanomaterials* 8 (12) (2018) 1038.
- [25] Z. Xu, D. Wu, Y. Liu, C. Liu, Z. Yu, L. Yu, H. Ye, Design of a tunable ultra-broadband terahertz absorber based on multiple layers of graphene ribbons, *Nanoscale Res. Lett.* 13 (1) (2018) 143.
- [26] D.R. Smith, R. Dalichaouch, N. Kroll, S. Schultz, S.L. McCall, P.M. Platzman, Photonic band structure and defects in one and two dimensions, *Josai Shika Daigaku Kiyō* 10 (2) (1993) 314–321.
- [27] D.R. Smith, D.C. Vier, Th. Koschny, C.M. Soukoulis, Electromagnetic parameter retrieval from inhomogeneous metamaterials, *Phys. Rev. E* 71 (3) (2005) 036617.
- [28] F. Fabregat-Santiago, Germà Garcia-Belmonte, Iván Mora-Seró, et al., Characterization of nanostructured hybrid and organic solar cells by impedance spectroscopy, *J. Chem. Soc. Faraday Trans.* 13 (20) (2011) 9083–9118.
- [29] D. Sievenpiper, L. Zhang, High-impedance electromagnetic surfaces with a forbidden frequency band, *IEEE Trans. Microw. Theory Tech.* 47 (11) (1999) 2059–2074.
- [30] Muntasir Hossain Md, Baohua Jia, Min Gu, A metamaterial emitter for highly efficient radiative cooling, *Adv. Opt. Mater.* 3 (8) (2015) 201500119.
- [31] Zhongyang Li, Serkan Butun, Koray Aydin, Ultranarrow band absorbers based on surface lattice resonances in nanostructured metal surfaces, *ACS Nano* 8 (8) (2014) 8242–8248.
- [32] Zachary J. Coppens, Wei Li, D. Greg Walker, Jason G. Valentine, Probing and controlling photothermal heat generation in Plasmonic Nanostructures, *Nano Lett.* 13 (2013) 1023–1028.
- [33] Pavlo Zolotavin, Alessandro Alabastri, Peter Nordlander, Douglas Natelson, Plasmonic heating in Au nanowires at low temperatures: the role of thermal boundary resistance, *ACS Nano* 10 (2016) 6972–6979.